University of Glasgow

Wen, L., Chen, Y., Liu, W., Su, Q., Grant, J. , Qi, Z., Wang, Q. and Chen, Q. (2017) Enhanced photoelectric and photothermal responses on silicon platform by plasmonic absorber and omni-schottky junction. *Laser and Photonics Reviews*, 11(5), 1700059.

There may be differences between this version and the published version. You are advised to consult the publisher's version if you wish to cite from it.

Wen, L., Chen, Y., Liu, W., Su, Q., Grant, J. , Qi, Z., Wang, Q. and Chen, Q. (2017) Enhanced photoelectric and photothermal responses on silicon platform by plasmonic absorber and omni-schottky junction. *Laser and Photonics Reviews*, 11(5), 1700059.(doi:10.1002/lpor.201700059)

This article may be used for non-commercial purposes in accordance with Wiley Terms and Conditions for Self-Archiving.

http://eprints.gla.ac.uk/145503/

Deposited on: 17 August 2017

Enhanced Photoelectric and Photothermal Responses on a Silicon Platform by an Integrated Plasmonic Absorber and Omni-Schottky Junction

Long Wen[1,2], Yifu Chen[1], Wanwan Liu[1], Qiang Su[1], Zhiyang Qi[3], Qilong Wang[3,*] and Qin Chen[1,2,*]

[1]Key Lab of Nanodevices and Applications, Suzhou Institute of Nano-Tech and Nano-Bionics, Chinese Academy of Sciences (CAS), Suzhou 215123, China; [2]Institute of Nanophotonics, Jinan University, Guangzhou 511443, China; [3]School of Electronic Science & Engineering, Southeast University, Nanjing 210000, China
*qchen2012@sinano.ac.cn or northrockwql@seu.edu.cn

Abstract

Recent progresses in plasmon-induced hot electrons open up the possibility to achieve photon harvesting effiiencies beyond the fundamental limit imposed by band-to-band transitions in semiconductors. To obtain high efficiency, both the optical absorption and electron emission/collection are crucial factors that need to be addressed in the design of hot electron devices. Here, we demonstrate a photoresponse as high as 3.3mA/W at 1500nm on a silicon platform using a plasmonic absorber (PA) and an omni-Schottky junction integrated photodetector, reverse biased at 5V and illuminated with 10mW. The PA fabricated on silicon consists of a monolayer of random Au nanoparticles (NPs), a wide-band gap semiconductor (TiO_2) and an optically thick Au electrode, resulting in broadband near-infrared (NIR) absorption and efficient hot-electron transfer via an all-around Schottky emission path. Time and spectral photoresponse measurements reveal that when the embedded NPs absorb the indicent radiation they act as local heating sources and transfer their energy to electricity via the photothermal mechanism, which until now has not been adequately assessed or rigorously differentiated from the photoelectric process in plasmon-mediated photon harvesting nano-systems

1. Introduction

The photovoltaic (PV) effect in semiconductors is the basic physical process converting photon energy to electricity. Relying on band-to-band transitions, a number of materials have been used over the past decades to address photodetection requirements across the electromagnetic spectrum, from the ultraviolet to mid-infrared [1]. With continuous shrinking of the feature size in modern integrated circuits, the integration of silicon photonics with electronic functionalities has emerged as the leading candidate to overcome electric interconnect bottleneck [2-4]. A vital challenge faced by silicon photonics is the design of efficient photodetectors integrated on silicon for the telecom regime. Since the photo-response of silicon undergoes cut-off around 1200 nm, epitaxial growth of relaxed germanium (Ge) or wafer bonding of III-V semiconductors on silicon is the commonly used method for achieving NIR photodetection on a silicon platform [5,6]. These approaches however have significant drawbacks such as thermal mismatch, the complexity in fabrication, high cost and integration issues. Aiming at all-silicon based NIR photodetection, trap-assisted absorption, two photon absorption and impurity-mediated sub-band gap response mechanisms have been investigated [7,8].

Parasitic plasmonic absorption has long been recognized as an energy loss process in many plasmonic optical or optoelectronic nanodevices [9-13] and is generally cosidered to be unwanted. However, on the flipside it offers the opportunity to effectively heat nanostructures and thus be useful in applications such as photothermal therapy [14]. Only receently has the parasitic absorption phenomena also been revealed to be useful for photon-to-electricity harvesting [15-26]. Associated with nonradiative plasmonic decay, the highly energetic electrons, also known as 'hot electrons', can be captured before thermalization by constructing a metal-semiconductor (M-S) Schottky junction or metal-insulator-metal (MIM) configuration. One of the most exciting aspects of hot electron harvesting is that a photoelectric response is induced if the hot carriers gain sufficient kinetic energy to overcome the energy barrier, without the limitations imposed by band-to-band transition of semiconductors. Realization of sub-band gap photodetection, spectral modulation [27] and imaging [28] on a silicon platform by plasmonic hot electrons is technically important for future chip-scale optoelectronic devices. Very recently, various plasmonic hot electron mediated on-chip and free-space photodetectors were proposed and demonstrated experimentally in the literature [29-36]. For instance, using the self-aligned approach of local oxidation of silicon (LOCOS) on a silicon-on-insulator substrate, a waveguide-based hot electron photodetector operating at telecom wavelengths has been demonstrated

exhibiting a responsivity of 12.5 mA/W [30]. Notably, by forming asymmetric MSM junctions on the side facets of the silicon waveguide, researchers have succeeded in obtaining a data repetition rate of 40 Gbit/s [32]. Such behaviour is possible on account of the ultrafast dynamics of the hot electron generation and injection. These silicon waveguide-based plasmonic photodetectors with strong mode confinement allow the guiding waves to propagate and be naturally absorbed adjacent to the Schottky interface and therefore enable efficient hot electron ejection. In contrast, free-space NIR photodetectors relying on the excitation of localized or propagating surface plasmons were realised by fabricating nano-antenna or metallic nano-gratings onto the silicon substrate [15,33,34]. However, inefficient optical absorption by the metallic emitters results in a relatively low responsivity and detectivity for such plasmonic hot electron devices. To this end, efforts have been made towards obtaining perfect absorption in the metal structures of hot electron based silicon photodetectors, This has been achieved by coating a thin layer of Au on the nano- or micro-structured silicon substrates [35,36]. With the elongated light-matter interaction path, perfect absorption in conjunction with an enhanced responsivity up to 1 mA/W in the range of 1250-1400 nm has been reported in deep silicon micro-trench supported Schottky devices [36]. To improve the electrical performance different device schemes relying on MIM tunneling [18] and embedding the M-S junction [34,37] have been proposed however strategies simultaneously optimising both the optical and electrical characteristics are urgently needed to achieve more efficient hot electron harvesting devices.

Besides the photoelectric hot electron emission process, the interband absorption in materials is also unavoidably accompanied by a photothermal process, which can be manifested as the photovoltaic or photoconductive response for optoelectronic devices operating in the NIR or even IR spectral range [38-42]. However, the photothermal response has rarely been discussed or discerned from the photoelectric effect in recent reported hot electron M-S photodetectors that show a response enhancement through external biasing [24,25]. Particularly, the relatively slow response on the order of tens of seconds or even minutes has been observed in some previous studies on hot electron devices [25].

Here, we present an approach by combining both optical and electrical perspectives into the design and experimental realization of a high performance plasmonic photodetector on a silicon platform. The proposed device contains Au nanoparticles (NPs) sandwiched between two electron-accepting semiconductors, TiO_2 and silicon, enabling high emission probability for the hot electrons due to the

formation of omni-directional M-S junctions. The plasmonic absorber (PA) based optical enhancing scheme is incorporated into a MSM configuration in order to obtain highly localized and perfect photon absorption in the mono-layered Au NPs. Exploiting benefits from embedding the plasmonic hot electron emitter [34] and PA [43-45] simultaneously, our results show that the proposed photodetector allows broad-band and perfect absorption along with a clear enhancement in both the hot electron and photothermal processes in the NIR regime. Through systematic investigations of the temporal response, the photoelectric and photothermal contributions to the total photoresponse were unequivocally distinguished.

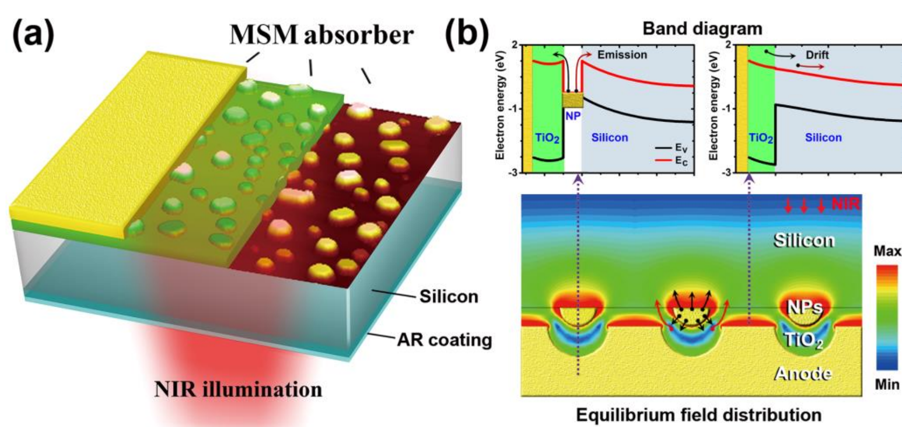

Figure 1. (a) Schematic drawings of the proposed PA integrated Si photodetectors. The typical morphology of the Au NPs formed via our thermal dewetting technique is depicted to enhance the illustration. (b) Energy band diagrams (top) and field distributions (bottom) under thermal equilibrium. The energy band alignments are sliced along the stacking direction of the MSM at two different positions.

2. Design principles and optoelectrical considerations for the PA integrated silicon photodetector

The proposed PA integrated photodetector is schematically illustrated in Fig. 1a. The trilayer PA structure fabricated on one side of silicon wafer consists of random Au NPs, an electron-accepting semiconductor and an optically thick Au reflector thatalso serves as the anode. Anti-reflection (AR) coatings are introduced on the other side of silicon substrate to suppress specular reflection loss. By tailoring the sizes, shapes and spatial distributions of the Au NPs, the PA structures can be readily designed to obtain broad-band and perfect plasmonic absorption in the NIR region where silicon is transparent. In addition, our optical studies indicate that the electromagnetic field is highly localized in the vicinity of Au NPs meaning that the photon absorption and therefore the hot electron excitation takes place mainly aorund the NPs.

In addition to considering the optical perfromance, the trilayer PA structure is also required to

promote hot electron ejection from the Au NPs. This was accomplished by employing a wide-band gap semiconductor, TiO_2, together with the underlying silicon as the electron-accepting semiconductor to fully surround the Au NPs. The feasibility of the PA device from an electrical standpoint was demonstrated with proof-of-principle calculations based on the drift-diffusion carrier transport framework (see Supporting Information S2 for details). As shown in Fig. 1b, at thermal equilibrium, there exists a high electric field distribution around the Au NPs due to the formation of a built-in electric potential adjacent to the M-S contact area. The photoexcited hot electrons with sufficient energy can therefore thermally emit into the surrounding electron-accepting materials and become majority carriers to be swept away from junctions. This process is highlighted by the corresponding energy band diagram plot (Fig. 1b, upper left). The reported electron affinity of the TiO_2 is around 4.0 eV [46] which is almost equal to the value of silicon, implying that there is no energy offset in the conduction band between TiO_2 and silicon. As depicted in the energy diagram (Fig. 1b, upper right), the whole PA structure resembles a Schottky diode. Thus, the hot electrons emitted into the TiO_2 can travel freely towards the cathode and contribute to photocurrents (the arrows in the band diagrams of Fig. 1b represent the drift flow of the emitted hot electrons), as they encounter the drift field posed by the rear Schottky contact. Moreover, the utilization of a wide-band gap semiconductor introduces a large valence band offset between TiO_2 and silicon which can be regarded as a hole-blocking barrier suppressing electron-hole recombination.

For the purpose of achieving broad-band plasmonic absorption, multiplexed plasmonic nano-antennas in a cascading form have been used [47] as an efficient way to extend the wavelengths of localized plasmonic responses. Instead of using lithography-based nano-fabrication, the metal thin-film thermal dewetting technique was employed to fabricate the Au NPs [44]. For the proposed PA structure shown in Fig. 1a, the size and filling ratio of the nano-antenna as well as the thickness of the TiO_2 loss-less cavity are critical parameters in determining the plasmonic resonance wavelength. To obtain high plasmonic absorption at the transparency window of silicon attelecom wavelengths, the optimal diameter of Au NPs is around 100-200 nm according to the optical simulations (see Supporting Information S4). The morphology of the Au NPs can be tuned in terms of their diameter and inter-spacing from several nanometers to micrometers via controlling the initial Au film thickness and the thermal dewetting process, thus providing great freedom to design a structure with the desired optical absorption properties. Figure 2a shows the morphologies of Au NPs prepared on silicon

substrates after being subjected to different dewetting temperatures. In general, increasing the dewetting temperature leads to a more uniform and well-defined size of Au NPs. For a temperature of 850 ℃, most of the Au NPs have a hexagonal shape. Accompanying the morphology evolution, the degree of crystallinity of Au NPs improves with increasing dewetting temperatures, as illustrated in Fig. 2b. It has been reported that metal nanostructures with improved crystalline quality can offer superior plasmonic properties compared to polycrystalline ones. Moreover, single-crystalline NPs with reduced grain boundaries could offer additional benefits in increasing the emission probability of the hot electrons. From the statistical analysis shown in Fig. 2c, Au NPs prepared by initial 14 nm Au thin-films and undergoing the dewetting process at 850 ℃ exhibit a size distribution with a large population in the range of 100-200 nm diameter, satisfying the requirement for obtaining broad-band NIR absorption.

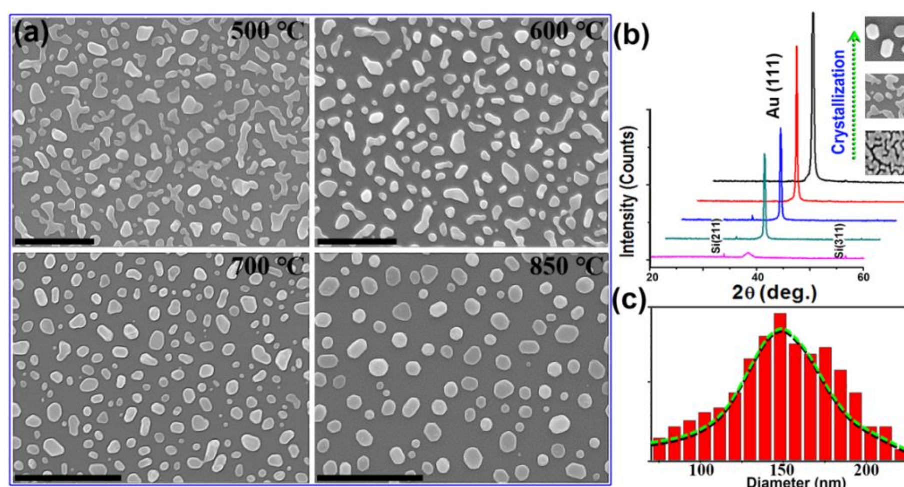

Figure 2. (a) Scanning electron microscopy (SEM) images of the Au NPs with different thermal dewetting temperatures. Thermal dewetting was performed in a rapid thermal processor (RTP) under nitrogen environment for 2 minutes. The initial mean thickness of the sputtered Au film is around 14 nm. The scale bar in each plot is 1 μm. (b) X-ray diffraction (XRD) patterns of themono-layer Au NPs on silicon substrates as a function of thermal dewetting temperature. The insert shows the morphology evaluation of Au NPs with increasing dewetting temperature. (c) Size histogram of the Au NPs prepared at 850 ℃ via statistical analysis.

Figure 3a shows the process flow for fabrication of the PA photodetectors. First, thin-film Au layers of different thicknesses were sputtered on the silicon substrate (n-type, 1-10Ω· cm). Note that the native oxide was not removed in order to give better dewetting behavior of Au films, as the thermal expansion coefficient of Si differs greatly from that of Au. After the 2 minute thermal dewetting process TiO_2 thin films were deposited onto the Au NPs using e-beam evaporation and then post-annealed in nitrogen at 400 °C for 2 hours. After annealing the TiO_2 has an optical band edge of

3.1 eV and is completely lossless in the NIR (see Supporting Information S3, Fig. S1a). Figure 3b shows the typical morphology of Au NPs before and after the TiO_2 deposition and post-annealing. The thermal annealing treatment does not change the NP distribution and shape but further facilitates the sidewall coverage of TiO_2 onto them. Next the rear Schottky and front ohmic electrodes were fabricated by sputtering thick layers of Au and Al respectively through a shadow mask. Finally, an AR coating comprised of 140 nm of silicon nitride and 100 nm of silicon dioxide was deposited via plasma-enhanced chemical vapor deposition. The AR coating suppresses the specular reflection loss to within 5% between 1150-1900 nm (Supporting Information S5).

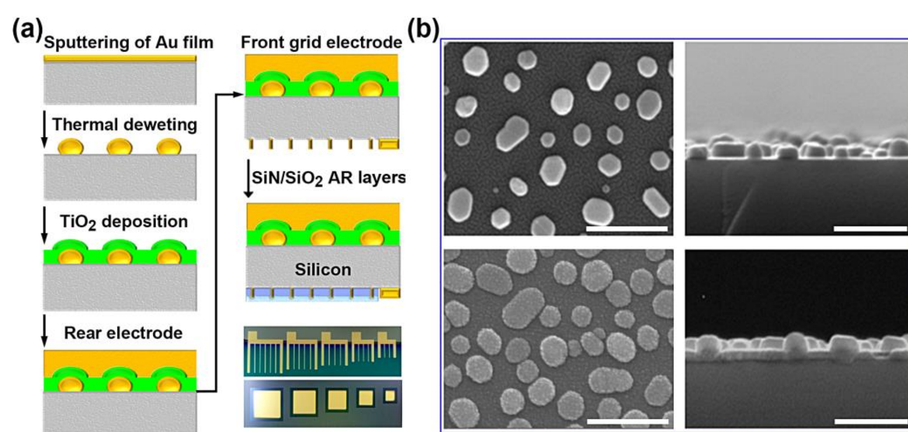

Figure 3. (a) Fabrication procedure for the PA photodetectors. The optical micrographs in the lower rightare the front side and back side views of five devices with different active areas (the smallest is $4mm^2$). (b) SEM images of the Au NPs before (top) and after deposition of the TiO_2 layer. Scale bar: 500 nm.

According to our optical simulations, the PAs with a fixed diameter of NPs (arranged in periodic square lattices) have a perfect absorption band in NIR with a FWHM of approximately 300 nm. The resonance wavelength depends mainly on the size of NPs if the thickness of TiO_2 remains constant (Supporting Information S4, Fig. S2b). The self-assembled Au NPs with random diameters and positions can therefore be regarded as independent nano-antennas with their resonances at geometry specific wavelengths. To quantitatively evaluate the collective response of the variation in NP diameter, numerically reconstructed PA using the realistic morphology of the Au NPs were studied via the three-dimensional FEM simulation, as shown in Figs. 4. The randomly distributed nano-antennas resembles to our previous cascading approach can significantly increase the bandwidth of PA response. As shown in Fig. 4d, broad-band absorption is obtained between 1200nm and 1800nm. The electric field distributions at three selected wavelengths are presented to explain the physical origin of the broadened PA absorption band with the simulation results also given in Fig. 4d. At short wavelengths,

it can be seen that the EM field is localized strongly around the small diameter NPs but moderately for the others. In contrast, at long wavelengths the EM coupling is prominent only for the larger NPs, resulting in weaker absorption. However, at the wavelength where the reflection minimum occurs, most of the NPs reveal a strong resonance character and therefore contribute to the high light absorption of the PA. In Fig. 4c, the power loss inside the PA is presented along with cross-sectional side-views of the complete structures. We see that most of the power is absorbed by the Au NPs and only a very small portion of light decays into the rear reflector. Nevertheless, it is significant to note that both the power absorption in NPs and rear reflector can contribute to the photocurrent.

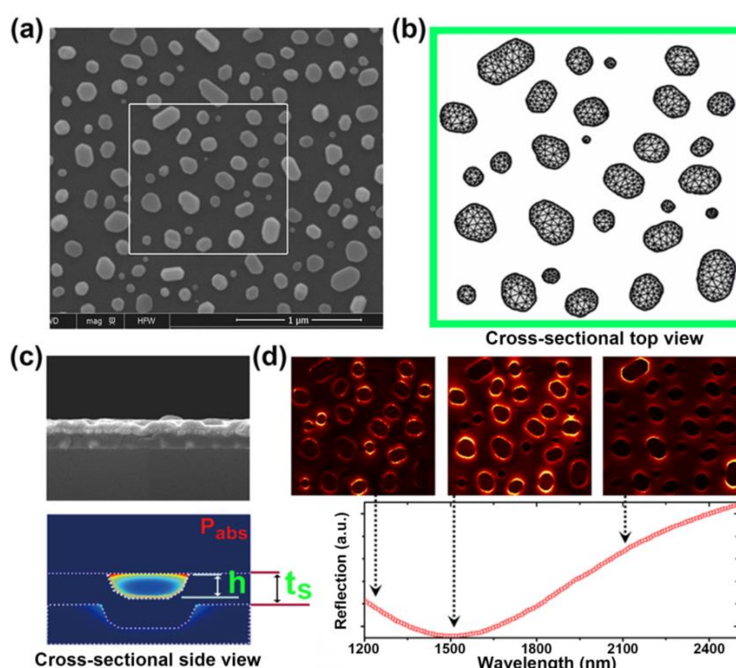

Figure 4. Optical simulations of PA structures using the realistic morphology of the random Au NPs. (a) SEM images of the Au NPs with optimized distributions for broad-band NIR plasmonic response. The white box represents the selected area to construct the optical models of the PA. (b) Cross-section in-plane views of the Au NPs with a self-adaptive mesh via finite-element method (FEM). (c) Side-view SEM images of the completed PA structures (top) and the cross-sectional side-view along with the normalized power absorbed per unit volume (Pabs) of the PA at a position where a NPs is present. A slightly tapered geometry of the NP was assumed in our simulation. The height of NPs is fixed to h=50 nm (average height of the prepared NPs) and thickness of TiO_2 is 60nm. (d) The simulated reflection spectra of the numerically reconstructed PA and the normalized electric field distributions plotted over an in-plane cross-section of the PA at three wavelengths.

3. Optical and electrical behaviour of the PA integrated devices

Experimental characterization of the optical performance of PA structures was performed and the results are summarized in Fig. 5a. Four PA structures containing Au NPs with different size distribution as well as a planar reference (absence of Au NPs) were fabricated and considered herein. The overall

dimensions including the diameter and inter-spacing of Au NPs can be efficiently tuned in the range of tens of nanometers to several hundred nanometers via selecting different initial Au film thickness. Generally, thinner initial Au films results in smaller diameters and inter-spacing distances and vice versa for the thicker initial Au thicknesses. Therefore, four initial Au films with mean thickness of 5, 8, 10, 14 nm were chosen to fabricate the PA structures shown in Fig. 5a. From the experimental absorption spectra, it is observed that the planar structure (AR/silicon/TiO_2/Au) has a very small absorption (around 10%) in the NIR region due to the highly reflective nature of the flat Au anode. In contrast, the introduction of Au NPs in the PA significantly improves the light absorption. Increasing the Au NPs size results in an obvious absorption enhancement and red-shift of the resonance band. The optimized PA (initial Au film thickness of 14 nm) has a remarkably high absorption in the wavelength range of 1300-1800 nm, thus satisfying the optical design requirement for the NIR photodetector.

The dark current-voltage (I-V) characteristics of Schottky devices can provide essential insights into the quality and barrier height of the M-S junctions that determine the efficiency and the cut-off wavelength of the hot electron conversion. Figure 5b shows the measured I-V curves of three photodetectors based on PA (with optimized Au NPs) and planar reference structures. Here, a PA device containing indium tin oxide (ITO) as the cavity material was also included (fabricated with same procedure as the TiO_2 based PA devices). For the planar reference and TiO_2 based PA devices, their electrical properties are mainly determined by the Au anode/TiO_2 M-S contact and both show a clear rectifying behavior in the I-V plot. However, the presence of Au NPs in the PA device slightly modifies the energy band alignment situation and also introduces a leakage path allowing the Au anode to electrically contact the silicon. As a result, the TiO_2 PA device tends to turn-on earlier than the planar device. For the ITO based PA device, the highly conductive ITO layer itself serves as the anode and forms a Schottky-like contact with silicon. Compared with the TiO_2 devices, it is found that the ITO based PA device has a relatively large reverse saturation current and lower turn-on voltage. This can be attributed to the smaller work function of ITO (4.8 eV) compared with Au (5.12 eV). To quantitatively determine the Schottky barrier of the three photodetectors, we fit the measured I-V curves in the forward voltage bias region to the Richardson-Schottky equation based on thermionic emission [48]. As illustrated in the logarithmic plot of Fig. 5b, the fitted curves are in good agreement with measured results for all three devices. The derived effective barrier heights of the planar reference, TiO_2 and ITO based PA devices are 0.89, 0.74 and 0.72 eV, respectively. The theoretical formula of the

fitting model and other derived electrical parameters can be found in Supporting Information S6.

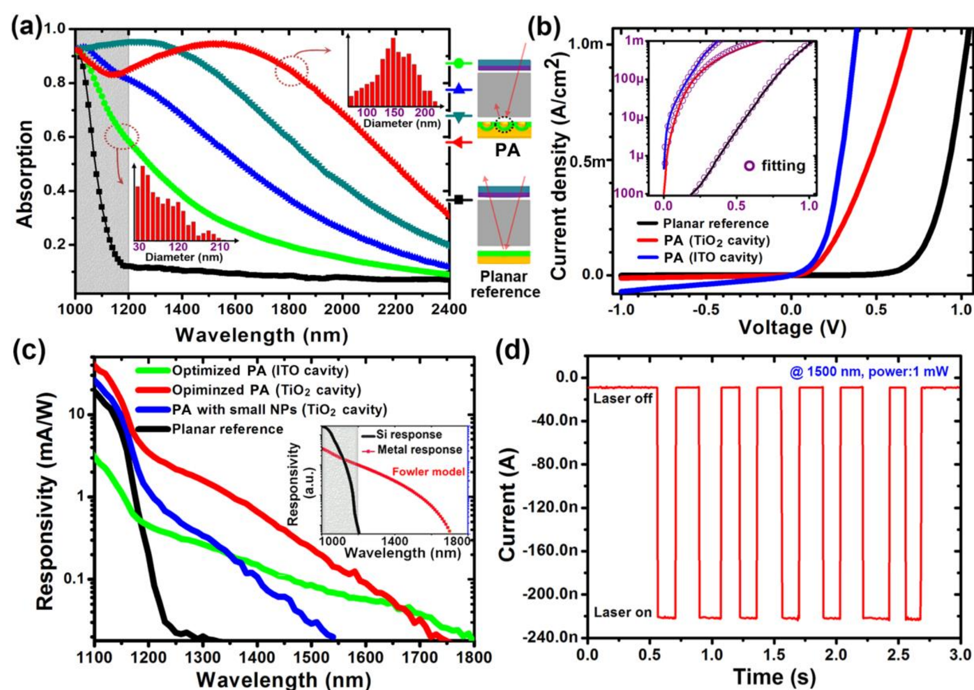

Figure 5. (a) The experimental absorption spectra of the PA structures with different particle sizes. The inset histograms illustrate the respective size distributions for two selected PAs with the smallest and largest NPs. The result for a planar reference device is also given. (b) Typical dark current-voltage curves for the PA and planar reference devices. PA devices consisting of TiO_2 and ITO as the cavity materials were considered. The inset shows a logarithmic plot where the fitted data (thermionic emission model, hollow circle) is also presented. (c) Responsivity of the different PA devices and planar device. The inset shows the theoretical results for two distinct response schemes. (d) The time-dependent current changes under fast switching of the laser illumination.

4. Spectral responsivity and omnidirectional hot electron emission of the PA integrated devices

We proceed now to fully evaluate the spectral harnessing potential of the proposed PA photodetectors. The photocurrent signal in response to chopped illumination (333Hz) was measured through the lock-in amplifier technique in the absence of external bias. Such a phase-sensitive detection set-up allows the contributions of the various photoresponse mechanisms to be distinguished, and importantly the ultrafast hot electron ejection process discerned against thermally induced responses. Figure 5c shows the measured spectral responsivity of various devices. All investigated devices reveal a high photoresponse at wavelengths shorter than about 1200nm, which is shown to be due to band-to-band transition related electron-hole pair generation in the silicon. Consistent with the optical absorption spectra, the planar reference device exhibits a dramatically decreased response near the cut-off wavelength of silicon. In contrast, the photoresponse of the PA devices can be divided into two wavelength regions (see Fig. 5c). For wavelengths below 1200nm the absorption is due to intrinsic loss

in the silicon while for wavelengths above 1200nm the absorption is due to the metallic PA. Contributions from the hot electron ejection can be distinguished by comparing the two TiO_2 based PA devices with the planar device. As direct evidence of the benefits of our optical design we observe that the optimized PA device has a higher responsivity compared to the PA with smaller NPs (initial thickness of Au for dewetting is 5 nm) which is in good agreement with their optical absorption characteristics. The TiO_2 based optimized PA device has a purely metallic response in the telecom wavelength range of 1300-1500 nm, with a responsivity ranging from 2.3 to 0.24 mA/W.

To provide a qualitative perspective of the observed photoresponse of the PA devices, a theoretical model based on the Fowler emission theory was adopted to reveal the spectral response potential of the hot electron ejection. The modified Fowler equation can be written as [34]: $Y = C_f A(h\nu - \Phi)^2/h\nu$, where, C_f is the Fowler emission coefficient, A is the experimental absorption spectra of the PA device, Φ is the Schottky barrier height and $h\nu$ is the energy of incident photon. With a weighted experimental absorption spectra term, the modified Fowler formula gives rise to a spectral responsivity shown in the inset of Fig. 5c. For the sake of simplicity we assumed that the Si response is proportional to the absorption spectra of a Si wafer with an AR coating which can be derived from its absorption coefficient. The resulting Si and metal spectral response determined from the above calculations are consistent with the experimental data revealing two distinct photoresponse mechanisms as discussed above. Notably, we observe that the simple Fowler model predicts a similar cut-off wavelength of the hot electron response as the experimental value. Further, the barrier height used herein is 0.71 eV, close to the previously determined value from the dark I-V curve of the TiO_2 MPA device.

In order to validate the enhancement of the hot electron ejection probability from the complete embedded absorber electrical design, we included a different control scenario, the ITO-based PA device (its dark I-V characteristics are detailed in Fig. 5b). This control device has similar high optical absorption properties as that of the TiO_2 PA devices (refer to Supporting Information S3 and S4) however its electrical characteristics are intrinsically different. The highly conductive and metallic-like ITO (carrier density ~ 10^{20} cm^{-3} according to Hall data) is more likely to form the M-S contact with silicon, but not the embedded Au NPs. As demonstrated in Fig. 5c, the proposed TiO_2 based PA device exhibits superior performance compared to the ITO scenario. For the TiO_2 PA structure, the Au NPs are switched by two semiconductors, both of which are excellent electron-accepting materials, hence resulting in an efficient omni-directional hot electron ejection. However, for the ITO control device,

only the hot electrons generated near the Au NPs/silicon M-S interface can be harvested, while those localized close to the NPs/ITO interface contribute to the ohmic losses. Finally, the replicability and stability of the proposed PA photodetector under alternately laser-on and laser-off illumination was examined. As confirmed in Fig. 5d, the hot electron mediated response remains unchanged after several cycles of on-off switching of the illumination and is capable of following the fast switching optical signal.

5. Distinguishing the Photoelectric and photothermal response in biased PA devices

In the above studies, the photodetectors were operated without external bias, where the hot electron was identified to be the dominant photoresponse mechanism. However, based on previous reports, other mechanisms can contribute, and in some cases even dominate the response in electrically biased interband photodetectors [7,8,38-42]. Among them, the photothermoelectric (PTE) [38,42] and bolometric effects [39-41] are more relevant in plasmonic device systems with both of these two mechanisms thermally driven. The former is known as the photo-thermoelectric or Seebeck effect which results in a built-in electric field allowing migration of the photoexcited carriers. The latter mechanism relies on local photothermal heating and also results in a reduction in the conductivity. Moreover, it should be also noted that electrically biased M-S or MIM junction can facilitate hot electron ejection. To evaluate the influence of these mechanism on the total photoresponse we studied a PA device operating under various external biasing conditions and a fixed illumination power of 10 mW.

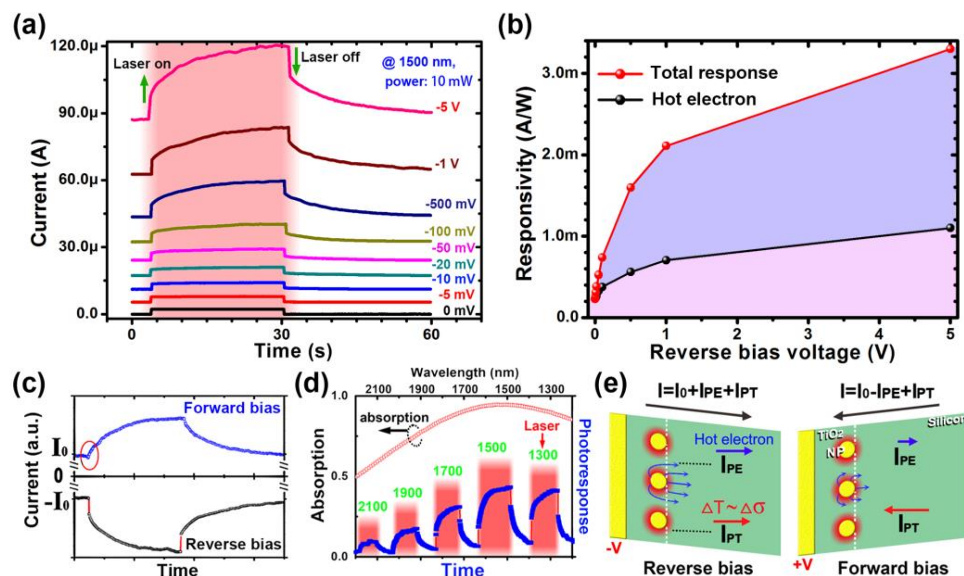

Figure 6. (a) Time-resolved photoresponse of the optimized PA photodetector at zero and various negative bias

voltages under steady laser illumination. (b) Photoresponsivity of the devices extracted from (a), the black line represents the fast hot electron response while the red line is the result after the photocurrent approaches saturation. (c) Time-resolved photoresponse of the PA photodetector applied with a large reverse bias (~5V) and small forward bias (~0.18V) under the same illumination conditions. These two voltage biases were chosen as they resulted in identical absolute dark current (I_0) values. (d) The time-resolved response under laser illuminations with various wavelengths along with the absorption spectra (red hollow circle, reproduced from Fig. 5a) of the reversely biased PA device. (e) Schematic drawing of the carrier transport dynamics of the hot electron and photothermally generated carrier under different applied drift fields.

Figure 6a shows the time-resolved photoresponse of the PA photodetector at various reverse bias voltages. We observe that when the device is reverse biased at small voltages (0~100 mV), after the laser is switched on, the current increases instantaneously and then remains steady until the illumination terminates. This behaviour implies that the response is dominated by the ultrafast hot electron process as we have detailed previously. However, one fascinating aspect that should be highlighted is the slightly improved photocurrent of the PA device in the presence of applied voltage. The enhancement of the hot electron related photoresponse becomes more apparent for larger reverse biases, manifested by the several times larger change in current at the initial stage (sub-second) of switching on or off the illumination, as compared to the results without bias. After the fast hot electron dynamic, the continuous light exposure on the PA device with large bias leads to a further increase in the photocurrent which takes tens of seconds before reaching a steady state, indicating the presence of the photothermally induced response. We extract the fast photocurrent (i.e. the hot electron response) and the total photocurrent (steady state) from Fig. 6a by subtracting the dark current and the resulting responsivity as a function of bias voltage which is plotted in Fig. 6b. For the hot electron related process, increasing the bias increases the responsivity. At a reverse bias of 5V, a responsivity of around 1.05 mA/W is observed for the hot electron component, which is four times larger than devices operating in the absence of an external voltage bias. The observed enhancement of the hot electron response can be largely attributed to the image force effects under a reverse bias which modify the barrier profile and improve the probability of hot electron ejection. In addition, the negative applied voltage on Au anode facilitates the migration of emitted hot electrons, especially for those generated in the TiO_2 cavity.

Taking into account the thermally induced component in Fig. 6b, we obtained the total photoresponse with a responsivity of 3.3 mA/W for the PA device reversely biased at 5 V. This photothermal response is also pronounced for the forward bias, as shown in Fig. 6c. In this plot, a large

reverse and a small forward bias was selected to ensure the PA device outputs dark currents with identical magnitude but opposite polarity. It is found that the photothermal response dominates upon illumination for a forward bias. However, a small dip (marked by the red circle) can be clearly resolved at the moment of illumination turn-on, which is due to the transient opposite photocurrent flow created by hot electron ejection. The magnitude of the photothermal photocurrent when the device is forward biased appears to be very close to the results of the slow response component when the device is reverse biased, implying an electrically driven origin. Regarding the photocurrent polarity, we can rule out involvement of the PTE process as it has a fixed polarity dependent on the direction of the internal built-in electric field. The bolometric mechanism, however, is a photoconductive response and exhibits the same polarity as the DC drive current regardless of the bias conditions. Together with the results shown in Fig. 6c, we can therefore safely classify the observed photothermal response to the bolometric effect. Under illumination, the superior absorption properties of the optimized PA results in efficient local heating at the MSM area and causes a temperature elevation across the device. Such a plasmonic heating effect increases the conductivity ($\triangle\sigma$) of the device and hence generates a thermalelectric-like response for the devices under external bias (the origin of the decrease in conductivity with increasing temperature of the Schottky devices will be discussed in the next section). Since it is highly dependent upon the temperature change, its spectral response appears to be in good agreement with the absorption spectrum of the PA and does not experience a responsivity cutoff in the investigated wavelength regime, as demonstrated in Fig. 6d. A conceptual description of the two distinct photoresponse processes observed for the PA devices operating under external bias conditions is presented in Fig. 6e. Under reverse bias, both the hot electron and the photothermal responses are enhanced and contribute to the photocurrent. While for forward bias, the hot electron photocurrent has the opposite polarity as the DC current flow but its magnitude is substantially decreased due to the raised emission barrier. In this case, the photothermal process exclusively dominates the photoresponse of the PA device. The observed photothermal signal stemming from diode bolometric effect has a slow response compared to previous micro-sized devices (on a time scale of ns~μs) [40,41], which is mainly attributed to the large size of our fabricated devices.

Fig.7a shows the dependence of the photoresponse on the incident power for the PA devices reversely biased at 5V (laser operation at a fixed wavelength 1500 nm). Over the experimentally accessible power range of our tunable laser, both the induced photoelectric and photothermal currents

increase almost linearly with increasing photon flux. The linear behavior of the hot electron response observed herein is consistent with previous reports [34,36], since it is dominated by the conversion of incident photons into hot electrons. In contrast, for the photothermal components, some non-linear effects might be expected to appear. The aforementioned rise in conductivity of the PA devices is driven by the modified thermal emission of M-S junction resulting from the elevated temperature. According to the thermal emission theory of an ideal Schottky diode, the saturation current density is given by $J_s=A^*T^2exp(-\Phi/kT)$ (A^* is Richardson constant, Φ is the barrier height and T is the temperature of device). The increase in the diode temperature modfies the total distribution of the electron energies in the Schottky electrode, resulting in a change of the saturation current. Thus, under reverse bias, the reverse current density ($-J_s$) is dominated by the thermal emission process and will increase in a non-linear manner with increasing device temperature. Such a non-linear relationship between the reverse current and temperature due to the modified thermal emission of M-S junctions was confirmed by performing I-V measurements on the PA devices in the temperature range of 27-47 °C, as shown in Fig. 7b. If we assume that the slow photon-response (refer to the photothermal current I_{PT}~23 μA for the incident power P~10 mW, inset of Fig. 7a) stems from photothermal heating, we obtain a temperature rise of approximately 6-7 °C for the device with 10 mW laser illumination according to the fitted △I~△T relationship (reverse bias 5V) shown in the inset of Fig. 7b. Thus, with such a small interval of temperature rise for the device illuminated with our experimentally accessible power range (0~10 mW), the non-linear behavior of its I_{PT}-P characteristic is not very prominent.

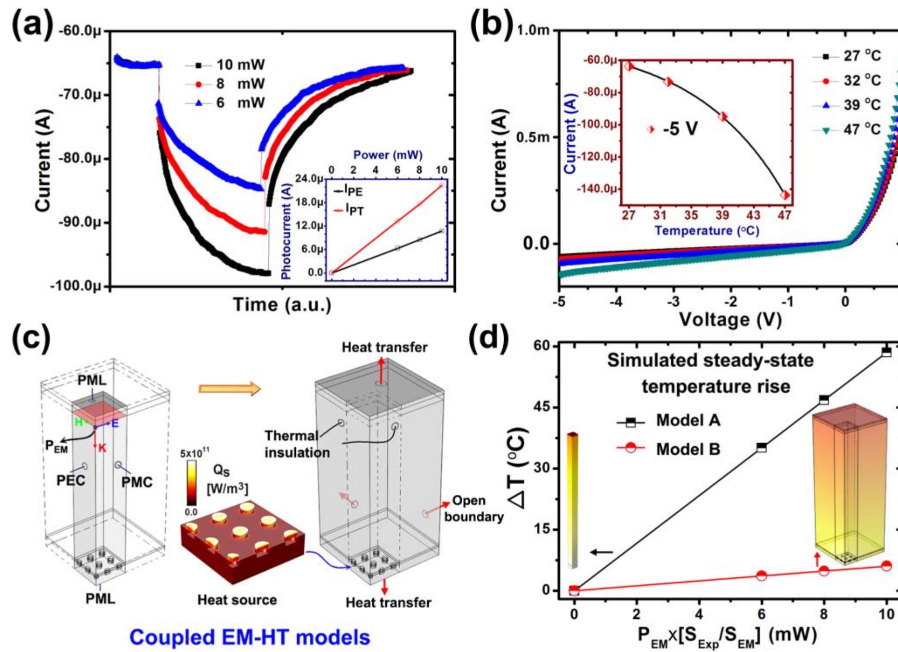

Figure 7. (a) Time dependent response of the PA integrated device illuminated with different incident powers. The inset shows the photoelectric and photothermal current versus the incident power. (b) I-V characteristics of PA device under different temperatures (heated in an oven). The inset shows the current dependence on temperature for a device with a negative bias of 5V. (c) Coupled EM-HT method for the modeling of the local heating effect of the PA device. In EM simulations, perfect magnetic conductor (PMC) and perfect electric conductor (PEC) boundaries were used to truncate the domain to one quarter of the full geometry containing the 5×5 NP array. The incident power density is estimated from experiments (laser power 4~10 mW, spot diameter~2.5 mm at 1500nm). In HT simulations, the combination of the thermal insulation and open boundaries allow us to mimic the effect of heat spreading over the non-illuminated device area and reduce the simulation volume to one quarter. (d) Calculated steady-state temperature elevation of PA device as a function of incident power. The insets show the temperature distribution in the simulated devices under steady-state (note that the temperature different across the device is smaller than 0.1 °C).

Finally, to give a quantitative measurement of the photothermal heating in the proposed PA integrated devices, we performed additional studies to analyze the temperature elevation for a given radiation power. Fully coupled EM-HT (electromagnetic wave - heat transfer) models in Comsol Multiphysics were developed for this purpose. The schematic of the multiphysics simulation model is shown in Fig. 7c. Both the simulation domains for the EM and HT calculations were reduced to one quarter by imposing appropriate boundary conditions in the side-facets. The EM-HT problem is solved for a finite illuminating area containing a 5×5 rectangular array of Au NPs. Individual NPs have a 150 nm diameter, arranged in a lattice of period 350 nm. As depicted in Supporting Information Fig. S2b, this periodic PA structure can absorb 85% of the incident radiation at 1500 nm. The resulting volumetric power absorption (Q_s, W/m^3) from the EM simulations is coupled to HT module as the heat source which eventually causes temperature elevation. In order to account for the spreading of the heat

to the surrounding areas not illuminated by the laser the simulation domain has been made larger in the HT domain compared to the EM domain and its side-facets are assigned to be open boundaries. At the front/rear facets of the HT domain we use a convective heat flux boundary condition driven by the temperature difference between the front/rear surfaces of the device and the surrounding atmosphere: $q=-h(T-T_{ext})$. Here q is the inward heat flux, T_{ext} is the ambient air temperature, and h (~10 W/m^2K) is the heat transfer coefficient for natural convection of air.

The calculated steady-state temperature elevation of the PA device as a function of incident power is shown in Fig. 7d. We also include a simplified model (labeled as model B) which ignores the effects of the heat spread over the non-illuminated device area. This model simulates a unit cell containing a single NP with thermal insulation boundaries imposed on all of the side-facets (the front/rear surfaces sremain convective). Thus, model B predicts the maximum attainable temperature rise for a device with the optimum thermal insulation design. Both model A and B (the complete EM-HT model shown in Fig. 7c) predict a linear-dependence of temperature rise withincident power. For calculated structures under the same power density as our experimental laser illumination with a power of 10 mW, model B gives rise to a temperature elevation of 6.05 °C, which is very consistent with the value (6-7 °C) we extracted from the inset of Fig. 7b. For the "thermally isolated' model A, the elevated temperature is around 58.5 °C, much higher than the value predicted by model B, thus identifying opportunities for further improvement in the photothermal response of our PA device.

6. Conclusions

In conclusion, we have proposed and successfully demonstrated an efficient MIR detectorbased on PA integrated silicon photodetectors. The easily fabricated PA is composed of a monolayer of random Au NPs and exhibits near-perfect and broad-band absorption at telecommunication wavelengths. Utilizing a MSM architecture to form the PA enables omnidirectional hot electron emission due to the formation of an all-around M-S contact between the plasmonic absorbers and electron-accepting semiconductors. By optimising both the optical and electrical properties of our MSM PA device, we experimentally show that the hot electron-mediated process provides significantly extended response beyond the silicon cut-off wavelength with responsivities up to 1.05 mA/W at 1500 nm for a reverse bias of 5V. In addition, the photothermally induced response arising from the plasmonic local heating effect further contributes to the performance of the PA photodetectors. The combination of the PA and

embedded nano-emitter on a silicon platform is a new design paradigm for realizing efficient on-chip NIR photodetection and imaging.

Acknowledgments

This work was supported by the grants from the National Natural Science Foundation of China (No. 11604367 and 61574158), the National Key Research and Development Program of China (No. 2016YFB0402501), the Key Frontier Scientific Research Program of the Chinese Academy of Sciences (No. QYZDB-SSW-JSC014), the Natural Science Foundation of Jiangsu Province (NO. BK20150369) and the Suzhou Science and Technology Development Program Foundation (No. SYG201529).

References

[1] A. Rogalski, Infrared Detectors, Second ed.; CRC Press: Boca Raton, FL (2011).

[2] M. Paniccia, Nat. Photon. **4**, 498-499 (2010).

[3] S. Borkar, and A. A. Chien, Commun. ACM **54**, 67-77 (2011).

[4] E. Timurdogan, C. M. Sorace-Agaskar, J. Sun, E. S. Hosseini, A. Biberman, and M. R. Watts, Nat. Commun. **5**, 1-11 (2014).

[5] J. Michel, J. Liu, and L. C. Kimerling, Nat. Photon. **4**, 527-534 (2010).

[6] J. Brouckaert, and D. Van Thourhout, J. Lightwave Technol. **25**, 1053-1060 (2007).

[7] M. Casalino, G. Coppola, R. M. De La Rue, and D.F. Logan, Laser Photon. Rev. **10**, 895-921 (2016).

[8] J. P. Mailoa, A. J. Akey, C. B. Simmons, D. Hutchinson, J. Mathews, J. T. Sullivan, D. Recht, M. T. Winkler, J. S. Williams, J. M. Warrender, P. D. Persans, M. J. Aziz, and T. Buonassisi, Nat. Commun. **5**, 3011 (2014).

[9] Q. Chen, X. Hu, L. Wen, Y. Yu, and D. R. S. Cumming, Small **12**, 4922-4935 (2016).

[10] Q. Chen, D. Das, D. Chitnis, K. Walls, T. D. Drysdale, S. Collins, and D. R. S. Cumming, Plasmonics **7**, 695-699 (2012).

[11] P. Berini, and I. De Leon, Nat. Photon. **6**, 16-24 (2012).

[12] V. E. Ferry, J. N. Munday, and H. A. Atwater, Adv. Mater. **22**, 4794-4808 (2010).

[13] L. Wen, Q. Chen, X. Hu, H. Wang, L. Jin, and Q. Su, ACS Nano **10**, 11076–11086 (2016).

[14] R. K. Kannadorai, and Q. Liu, Med Phys. **40**, 103301 (2013).

[15] M. W. Knight, H. Sobhani, P. Nordlander, and N. J. Halas, Science **332**, 702-704 (2011).

[16] B. Du, L. Lin, W. Liu, S. Zu, Y. Yu, Z. Li, Y. Kang, H. Peng, X. Zhu, and Z. Fang, Laser Photonics Rev. **11**, 1600148 (2017).

[17] Y. Yu, Z. Ji, S. Zu, B. Du, Y. Kang, Z. Li, Z. Zhou, K. Shi, and Z. Fang, Adv. Funct. Mater. **26**, 6394–6401 (2016).

[18] F. Wang, and N.A. Melosh, Nano Lett. **11**, 5426-5430 (2011).

[19] F. Wang, and N.A. Melosh, Nat. Commun. **4**, 1711 (2013).

[20] C. Clavero, Nat. Photon. **8**, 95-103 (2013).

[21] H. Chalabi, D. Schoen, and M. L. Brongersma, Nano Lett. **14**, 1374–1380 (2014).

[22] A. Manjavacas, J.G. Liu, V. Kulkarni, and P. Nordlander, ACS Nano **8**, 7630–7638 (2014).

[23] M.L. Brongersma, N.J. Halas, and P. Nordlander, Nat. Nanotechnol. **10**, 25-34 (2015).

[24] F. P. Garcia de Arquer, A. Mihi, and G. Konstantatos, ACS Photonics **2**, 950–957 (2015).

[25] H. S. Kojori, J. Yun, Y. Paik, J. Kim, W. A. Anderson, and J. S. Kim, Nano Lett. **16**, 250–254 (2016).

[26] K. Wu, Y. Zhan, S. Wu, J. Deng, and X. Li, J. Appl. Phys. **118**, 063101 (2016).

[27] M. Abb, P. Albella, J. Aizpurua, and O.L. Muskens, Nano Lett. **11** 2457–2463 (2011).

[28] Y. Ho, L. Huang, and J. Delaunay, Nano Lett. **16**, 3094–3100 (2016).

[29] A. Akbari, R.N. Tait, and P. Berini, Opt. Express **18**, 8505-8514 (2010).

[30] I. Goykhman, B. Desiatov, J. Khurgin, J. Shappir, and U. Levy, Nano Lett. **11**, 2219-24 (2011).

[31] S. Ishii, S. Inoue, R. Ueda, and A. Otomo, ACS Photonics **1**, 1089-1092 (2014).

[32] S. Muehlbrandt, A. Melikyan, T. Harter, S. Köhnle, A. Muslija, P. Vincze, S. Wolf, P. Jakobs, Y. Fedoryshyn, W. Freude, J. Leuthold, C. Koos, and M. Kohl, Optica **7**, 741-747 (2016).

[33] A. Sobhani, M. W. Knight, Y. Wang, B. Zheng, N. S. King, L. V. Brown, Z. Fang, P. Nordlander, and N. J. Halas, Nat. Commun. **4**, 1643 (2013).

[34] M. W. Knight, Y. Wang, A. S. Urban, A. Sobhani, B. Y. Zheng, P. Nordlander, and N. J. Halas, Nano Lett. **13**, 1687-1692 (2013).

[35] W. Li, and J. Valentine, Nano Lett. **14**, 3510-3514 (2014).

[36] K. T. Lin, H. L. Chen, Y.S. Lai, and C. C. Yu, Nat. Commun. **5**, 3288 (2014).

[37] Z. Fang, Z. Liu, Y. Wang, P.M. Ajayan, P. Nordlander, and N.J. Halas, Nano Lett. **12**, 3808-3813 (2012).

[38] M. Buscema, M. Barkelid, V. Zwiller, H. S. J. van der Zant, G. A. Steele, and A. Castellanos-Gomez, Nano Lett. **13**, 358–363 (2013).

[39] N. Kurra, V. S. Bhadram, C. Narayanaa, G. U. Kulkarni, Nanoscale **5**, 381-389 (2013).

[40] M. H. Kim, J. Yan, R. J. Suess, T. E. Murphy, M. S. Fuhrer, and H. D. Drew, Phys. Rev. Lett. **110**, 247402 (2013).

[41] N. Youngblood, C. Chen, S. J. Koester, and M. Li, Nat. Photonics **9**, 249 (2015).

[42] Y. Lai, C. Tsai, C. Chang, C. Huang, V.K.S. Hsiao, and Y. Oliver Su, Adv. Mater. **28**, 2644–2648 (2016).

[43] J. Hao, L. Zhou, and M. Qiu, Phys. Rev. B **83**, 165107 (2011).

[44] K. Liu, X. Zeng, S. Jiang, D. Ji, H. Song, N. Zhang, and Q. Gan, Nanoscale **6**, 5599-5605 (2014).

[45] X. Hu, G. Xu, L. Wen, H. Wang, Y. Zhao, Y. Zhang, D.R.S. Cumming, and Q. Chen, Laser photonics Rev. **10**, 962-969 (2016).

[46] X. Yin, C. Battaglia, Y. Lin, K. Chen, M. Hettick, M. Zheng, C.Y. Chen, D. Kiriya, and A. Javey, ACS Photonics **1**, 1245-1250 (2014).

[47] L. Wen, F. Sun, and C. Chen, Appl. Phys. Lett. **104**, 151106 (2014).

[48] H. Norde, J. Appl. Phys. **50**, 5052-5053 (1979).